

## RESEARCH ARTICLE

10.1029/2018JB015995

## Key Points:

- Crustal anisotropy in southeastern Tibet and adjacent areas is measured at 208 seismic stations using moveout of *P* to *S* receiver functions
- Magnitude of anisotropy on the plateau is twice of that in the Sichuan Basin, and the orientation is mostly consistent with fault strike
- Along-strike variation of anisotropy in the Longmenshan fault zone is related to extensional cracks, lower crustal flow, and fluid filled fractures

## Supporting Information:

- Supporting Information S1
- Table S1
- Table S2

## Correspondence to:

S. S. Gao,  
sgao@mst.edu

## Citation:

Zheng, T., Ding, Z., Ning, J., Chang, L., Wang, X., Kong, F., et al. (2018). Crustal azimuthal anisotropy beneath the southeastern Tibetan Plateau and its geodynamic implications. *Journal of Geophysical Research: Solid Earth*, 123. <https://doi.org/10.1029/2018JB015995>

Received 20 APR 2018

Accepted 5 OCT 2018

Accepted article online 11 OCT 2018

## Crustal Azimuthal Anisotropy Beneath the Southeastern Tibetan Plateau and its Geodynamic Implications

Tuo Zheng<sup>1,2,3</sup>, Zhifeng Ding<sup>1</sup>, Jieyuan Ning<sup>2</sup>, Lijun Chang<sup>1</sup>, Xingchen Wang<sup>1</sup> , Fansheng Kong<sup>3,4</sup>, Kelly H. Liu<sup>3</sup> , and Stephen S. Gao<sup>3</sup> 

<sup>1</sup>Institute of Geophysics, China Earthquake Administration, Beijing, China, <sup>2</sup>School of Earth and Space Sciences, Peking University, Beijing, China, <sup>3</sup>Geology and Geophysics Program, Missouri University of Science and Technology, Rolla, MO, USA, <sup>4</sup>Key Laboratory of Submarine Geosciences, Second Institute of Oceanography, State Oceanic Administration, Hangzhou, China

**Abstract** The fast orientation and magnitude of crustal azimuthal anisotropy beneath the southeastern Tibetan Plateau and adjacent areas are measured by analyzing the sinusoidal moveout of the *P* to *S* converted phase from the Moho. Beneath the tectonically active plateau, the mean magnitude is  $0.48 \pm 0.13$  s, which is about twice as large as that observed in the stable Sichuan Basin ( $0.23 \pm 0.10$  s). The two areas are separated by the Longmenshan fault zone, a zone of devastating earthquakes including the 12 May 2008  $M_w$  7.9 Wenchuan earthquake. Fault orthogonal fast orientations observed in the southern Longmenshan fault zone, where previous studies have revealed high crustal  $V_p/V_s$  and suggested the presence of mid-lower crustal flow, may reflect flow-induced lattice preferred orientation of anisotropic minerals. Fault parallel anisotropy in the central segment of the fault zone is most likely related to fluid filled fractures, and fault perpendicular extensional cracks are probably responsible for the observed anisotropy in the northern segment. The crustal anisotropy measurements, when combined with results from previous studies, suggest the existence of mid-lower crustal flow beneath the southeastern margin of the plateau. Comparison of crustal anisotropy obtained before and after the Wenchuan earthquake suggests that the earthquake has limited influence on whole crustal anisotropy, although temporal changes of anisotropy associated with the earthquake have been reported using splitting of shear waves from local earthquakes occurred in the upper crust.

## 1. Introduction

It is generally accepted that the Tibetan Plateau is the consequence of progressive continental collision between the Indian and Eurasian plates initiated some 70 Ma ago (Molnar & Tapponnier, 1975). In spite of numerous studies, the mechanisms responsible for the lateral expansion of the plateau remain debated. The area adjacent to the eastern and southeastern margins of the plateau (Figure 1), including the tectonically active Songpan-Ganzi-Kangding (SGK) and the Dianzhong blocks, and the relatively stable Yangtze Platform which is mainly composed of the Sichuan Basin in the study area, is an ideal locale to explore processes related to crustal deformation in response to continental collision. The actively deforming plateau is separated from the stable Sichuan Basin by the Longmenshan (LMS) fault zone, which is seismically one of the most active regions in China (Ma, 2002; H. Zhang et al., 2016). A number of great earthquakes, including the 2008  $M_w$  7.9 Wenchuan and the 2013  $M_s$  7.0 Lushan earthquakes, have occurred in the LMS fault zone since the 1970s.

Many geodynamic models have been proposed to explain the deformation and uplift of the southeastern Tibetan Plateau, and three of them have attracted the most attention, including motion of rigid crustal blocks along major fault zones (Tapponnier et al., 1990, 2001), crustal shortening and thickening due to coherent lithospheric deformation (Copley, 2008; England & Houseman, 1986; Silver, 1996; C.-Y. Wang et al., 2008), and ductile channel flow in the mid-lower crust (Clark & Royden, 2000; Royden et al., 1997). While it has recently been recognized that for a given area, more than one of the proposed mechanisms may operate (e.g., Bendick & Flesch, 2007; Q. Liu et al., 2014; Yang & Liu, 2009), the relative importance of those mechanisms remains controversial.

It has long been recognized that seismic azimuthal anisotropy can provide important insights into the strain occurring at depth (Crampin et al., 1980; Lev et al., 2006; Mainprice & Nicolas, 1989), and thus can provide

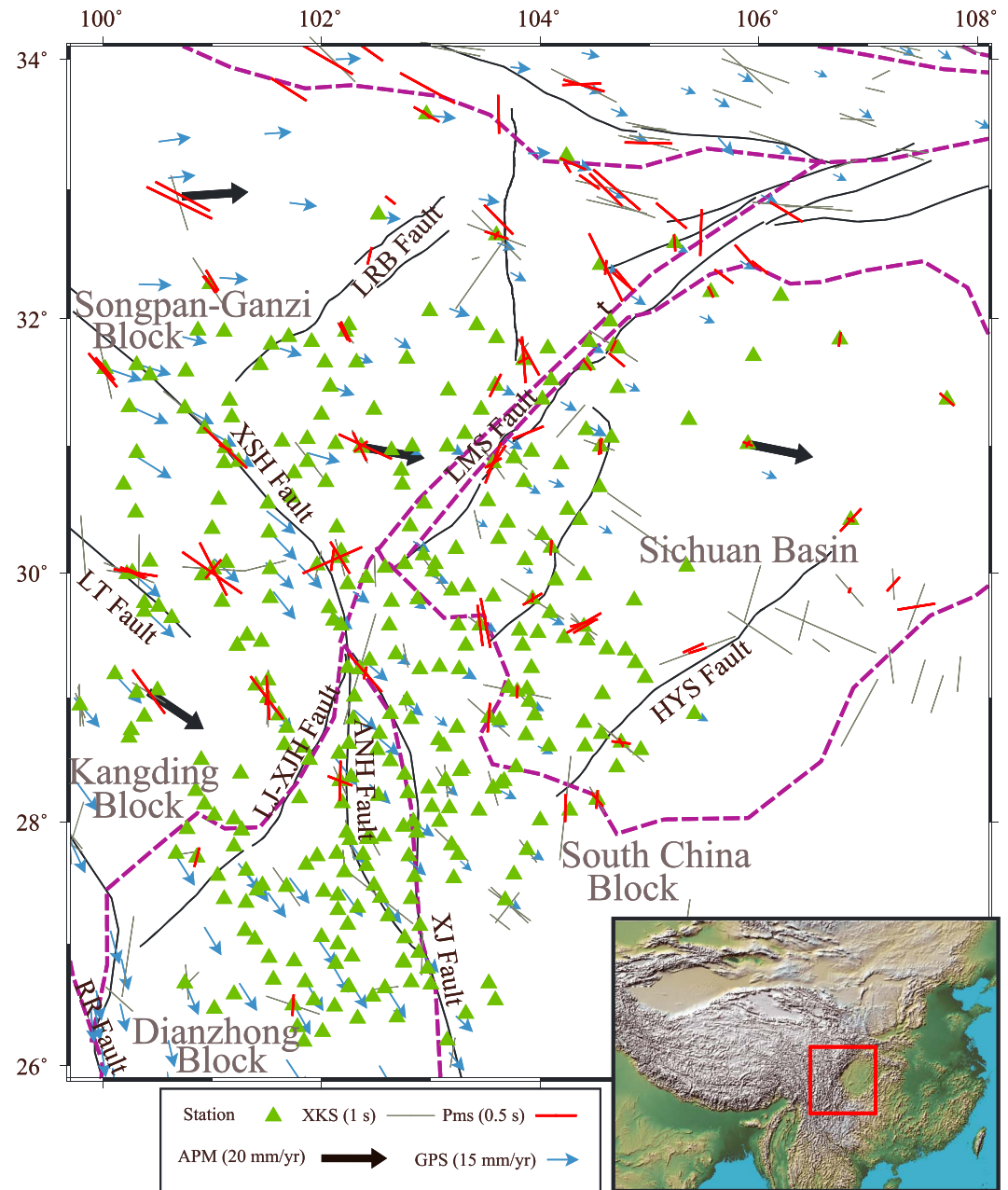


**Figure 1.** A topographic relief map of the southeastern Tibetan Plateau and adjacent areas showing stations used in this study (green triangles), major geological boundaries (dashed purple lines), and major faults (solid black lines). The light blue arrows indicate GPS velocities (Gan et al., 2007) with respect to the stable Eurasia, and the thick black arrows represent the APM derived from the GSRM-APM-1 model (Kreemer, 2009). The red bars show previous crustal anisotropy measurements (Chen et al., 2013; Kong et al., 2016; Sun et al., 2015), and the thin gray bars are XKS splitting results obtained from <http://splitting.gm.univ-montp2.fr/DB/public/searchdatabase.html>. The solid red rectangle in the inset map indicates the location of the study area. Faults: ANH = Anninghe; HYS = Huayingshan; LJ-XJH = Lijiang-Xiaojinhe; LMS = Longmenshan; LRB = Longriba; LT = Litang; RR = Red River; XJ = Xiaojiang; XSH = Xianshuihe.

important constraints on the geodynamic models for the uplifting and lateral expansion of the Tibetan Plateau. As a proxy for subsurface deformation at depth, seismic azimuthal anisotropy is generally quantified by two parameters, including the fast orientation ( $\phi$ ) and magnitude ( $\delta t$ ) of the transversely isotropic medium (Crampin, 1987; Silver, 1996). In the upper crust, azimuthal anisotropy is mostly produced by microcracks (Crampin & Peacock, 2008; McNamara & Owens, 1993); and in the mid-lower crust beneath areas without deep faults, due to the closure of the cracks, anisotropy is mainly caused by the lattice preferred orientation

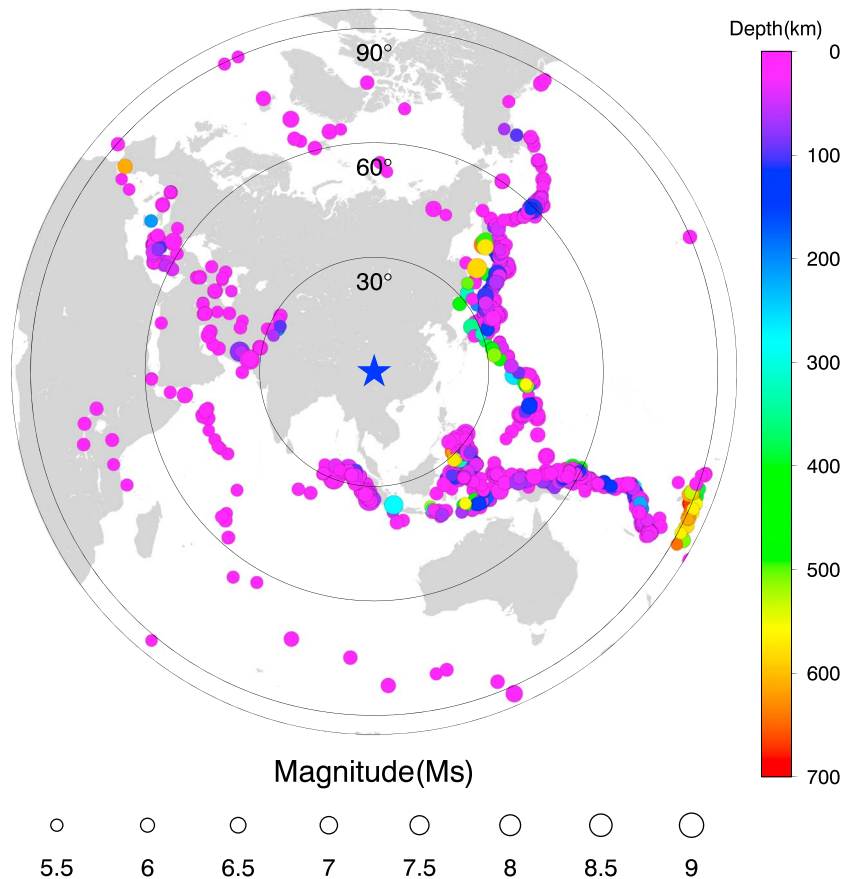


**Figure 2.** Distribution of teleseismic events used in the study. The circles representing the events are color coded by the focal depths, and the magnitudes are proportional to the size of the circles. The blue star indicates the center of the study area.

(LPO) of anisotropic minerals, primarily amphibole (Meissner et al., 2002; Tatham et al., 2008). Recent studies suggested that amphibolite symmetry is dependent on deformation type (Brownlee et al., 2017; Ji et al., 2013, 2015), and the types of amphibole fabrics are related to the differential stress and temperature (Ko & Jung, 2015; Kong et al., 2016). Under the conditions of high temperature and differential stress that are typical for the thickened crust on the Tibetan Plateau, fast orientations are expected to be subparallel to the flow direction (Kong et al., 2016).

In the study area (Figure 1), source-normalized  $P$  to  $S$  converted waves from the Moho ( $P_{ms}$ ), which are termed as receiver functions (RFs), have been utilized by several studies to characterize crustal azimuthal anisotropy (Figure 1). Chen et al. (2013) analyzed  $P_{ms}$  splitting from individual RFs and obtained an average splitting time of about 0.19 s at 98 stations located in Sichuan and Yunnan Provinces, China. The  $P_{ms}$  splitting times are much smaller than those obtained using the XKS phases (including SKS, PKS, and SKKS), which are  $P$  to  $S$  converted phases from the core mantle boundary, and thus the resultant splitting parameters represent the integrated anisotropy along the ray path from the core mantle boundary to the surface (Figure 1). Their measurements suggested the presence of a lower crustal flow system which is obstructed by the Dianzhong Block and supported a mechanically decoupled model between the upper crust and the mantle lithosphere beneath the southeastern Tibetan Plateau. Sun et al. (2012) used a harmonic analysis method to suggest that crustal anisotropy has an important contribution to XKS splitting. Sun et al. (2015) speculated that uplifting of the LMS fault zone was the result of lower crustal flow extrusion and supported a coupled deformation model from the lower crust to upper mantle underneath the LMS fault zone. Kong et al. (2016) utilized moveout time variations of the  $P_{ms}$  phase to suggest that crustal thickening is the main mechanism of the high topographic gradient across the LMS Fault, a conclusion that is inconsistent with that from Sun et al. (2015).

Previous crustal anisotropy studies using RFs (e.g., Chen et al., 2013; Kong et al., 2016; Sun et al., 2012, 2015) have provided invaluable information on crustal structure and deformation beneath the southeastern Tibetan Plateau and adjacent areas. However, considerable discrepancies are present among those studies (Figure 1). More importantly, significantly different conclusions regarding a number of essential geodynamic problems, such as the mechanisms responsible for the surface uplift of the LMS fault zone, crustal flow paths, and coupling or decoupling between shallow and deep structures, have been reached by the previous studies. These controversies are mostly due to the limited number of stations and the large (relative to this study) station spacing used in previous studies. Another significant issue that has not been addressed by previous studies is whether large earthquakes such as the 2008  $M_w$  7.9 Wenchuan Earthquake, which ruptured the central and northern segments of the LMS Fault (Shen et al., 2009; H. Zhang & Ge, 2010), can modify crustal anisotropy. Pre- and post-earthquake differences in seismic anisotropy in the upper crust have been documented by splitting analysis of direct  $S$  waves from local earthquakes occurred in the upper crust (e.g., Chang et al., 2014; Crampin et al., 1999; Crampin & Zatsepin, 1997; Ding et al., 2008). However, possible influences of the earthquake on whole crustal anisotropy have not been investigated.

This study takes advantage of a unique data set recorded by a dense portable array and several permanent networks to characterize crustal anisotropy beneath the southeastern Tibetan Plateau and adjacent areas with unprecedented spatial coverage and resolution. It is aimed at providing additional constraints on crustal thickening and surface uplifting models and to investigate possible effects of the Wenchuan earthquake on whole crustal anisotropy.

## 2. Data

Data used in this study were recorded by 344 broadband seismic stations (Figure 1) located on the southeastern Tibetan Plateau and the neighboring Yangtze Platform, among which 284 stations belong to the Temporary Western Sichuan Array deployed between 2006 and 2009. Each of the Temporary Western Sichuan Array stations was instrumented with a Guralp CMG-3ESPC (60 s–50 Hz) sensor and a REFTEK-130B01 recorder, and the interstation distance was 10–30 km. Additionally, data from 60 permanent Sichuan provincial seismic stations were obtained for the period between 2010 and 2014. These stations were equipped with two types of sensors: CMG-3ESPC and CMG-3ESPB (60 s–50 Hz). A total of 968 teleseismic events with magnitudes greater than  $M_s$  5.5 within the epicentral distance range of 30–90° were selected. All the teleseismic events were band-pass filtered in the frequency range of 0.02 to 1.0 Hz. These events provide a reasonably good back-azimuthal coverage (Figure 2).

## 3. Methods

### 3.1. Calculation of RFs

In order to generate the RFs, the two horizontal components of the filtered seismograms are rotated into radial (R) and transverse (T) components. The time-domain iterative deconvolution technique (Ligorria & Ammon, 1999) is employed to compute the RFs. A Gaussian low-pass filter with a Gaussian width factor of 2.5 Hz is utilized to further remove high-frequency noise. A signal-to-noise ratio (SNR) RF selection procedure (S. S. Gao & Liu, 2014) is applied to reject low-quality RFs. A total of 38,248 radial RFs are retained at 344 stations, with the number of RFs per station ranging from 45 to 188.

### 3.2. Measurement of Single Layered Anisotropy

Crustal anisotropy has been investigated using various techniques such as shear wave splitting from local earthquakes (Crampin & Gao, 2008), splitting of  $P$  to  $S$  conversions from the Moho (McNamara & Owens, 1993), and systematic moveout of the  $P$  to  $S$  conversions (Levin & Park, 2000; H. Liu & Niu, 2012; Z. Liu et al., 2015; Z. Liu & Park, 2017; Rumpker et al., 2014). An array of assumptions including a single layer with a horizontal axis of symmetry (Kong et al., 2016; Sun et al., 2012, 2015), several horizontal layers (Z. Liu et al., 2015; Z. Liu & Park, 2017), and a single dipping layer (Frederiksen & Bostock, 2000; Shiomi & Park, 2008) have been applied in the studies. This study aims at quantifying the bulk crustal anisotropy under the assumption of a horizontal symmetry axis and a flat interface (e.g., Kong et al., 2016; H. Liu & Niu, 2012; Nagaya et al., 2008; Rumpker et al., 2014; Sun et al., 2012) using a unique data set recorded by a large (relative to similar studies in the area) number of stations in a tectonically significant area. Assuming a single layer of anisotropy with a horizontal axis of symmetry and a flat Moho, the arrival time of the  $P_m$ s shifts systematically as a cosine function of the

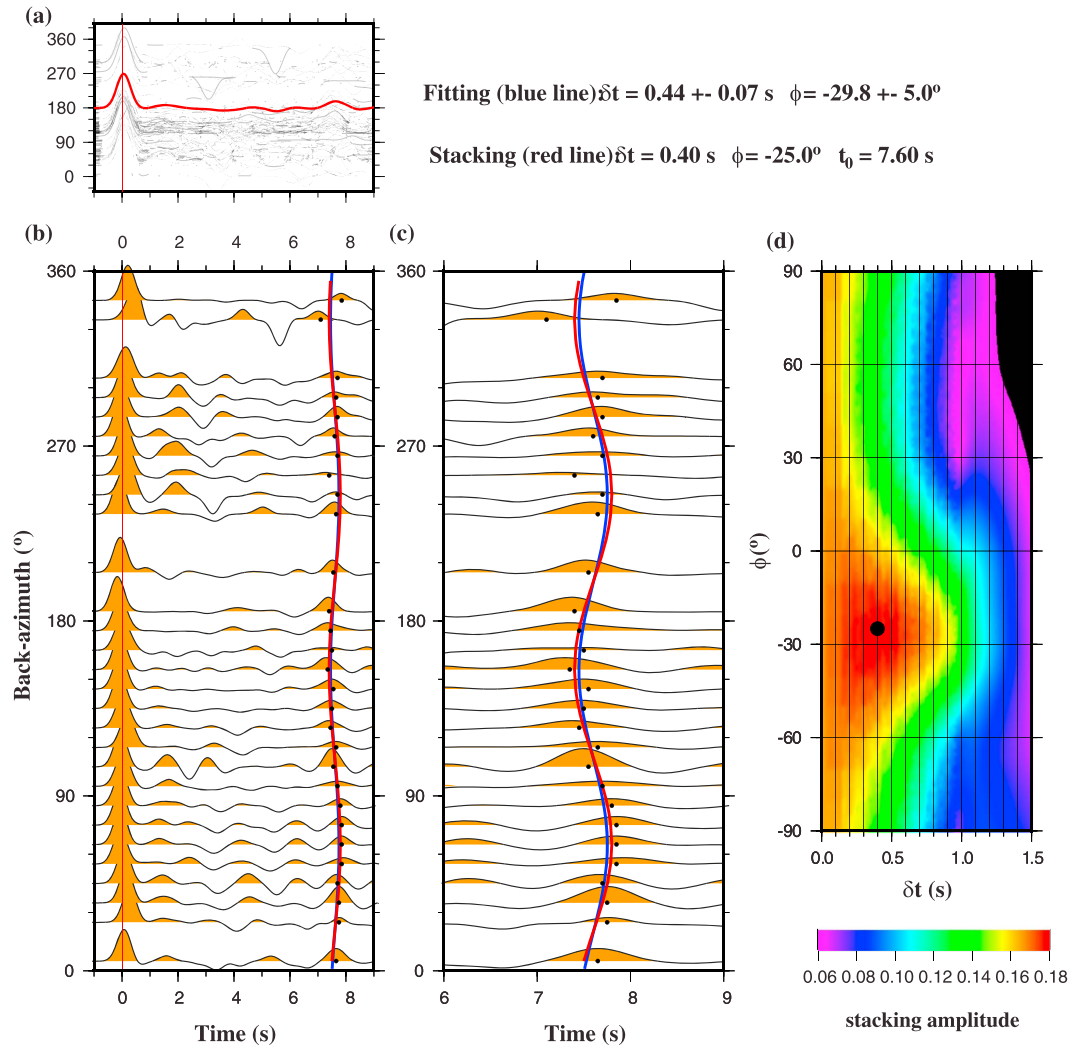


**Figure 3.** Crustal anisotropy measurements at station KXL01 (100.24°E, 31.31°N). (a). Original RFs. The red trace shows the result of simple time-domain summation of the individual RFs. (b). Back azimuth band averaged RFs plotted against the back azimuth. The dot on each of the traces indicates the  $P_m$ s arrivals. The red curve is the theoretical moveout calculated based on the optimal anisotropy parameters revealed in (d), and the blue curve is that obtained by fitting the  $P_m$ s moveout using equation (1). Note that all the RFs are corrected to a uniform equivalent epicentral distance of 60° and a source depth of 0 km. (c). Same as (b) but for the time window of 6–9 s. (d). Stacking amplitudes corresponding to all the candidate pairs of the anisotropy parameters. The black dot denotes the optimal pair of parameters associated with the maximum stacking amplitude. RFs = receiver functions.

back azimuth (BAZ; H. Liu & Niu, 2012; Rumpker et al., 2014), that is,

$$t = t_0 + \Delta t = t_0 - \frac{\delta t}{2} \cos[2(\phi - \theta)], \quad (1)$$

where  $t_0$  denotes the arrival time in the isotropic model,  $\Delta t$  represents the moveout of the arrival times due to crustal azimuthal anisotropy along the ray path,  $\delta t$  reflects the magnitude of anisotropy and is equivalent to the delay time between the fast and slow shear waves in shear wave splitting analysis,  $\phi$  is the fast orientation (measured clockwise from the north) along which the  $P_m$ s has the earliest arrival and is equivalent to the fast polarization orientation in shear wave splitting analysis, and  $\theta$  is the BAZ of the incoming ray. Obviously, the azimuthal variation of the moveout has a 180° periodicity. The same technique can also be applied to  $P_t$ s, which is the  $P$  to  $S$  conversion from an intracrustal interface that is clearly observable at a few stations, to quantify anisotropy above the interface.

Prior to applying equation (1), we take the following steps to preprocess and select the RFs. (a). Moveout correction (Kong et al., 2016). The RFs are corrected to a uniform equivalent epicentral distance of 60° and source

depth of 0 km so that the effects of the variations of  $P_{m,s}$  arrival times associated with epicentral distance variations can be excluded. (b). Stacking the corrected traces. To enhance the SNR, RFs in the same BAZ band of  $10^\circ$  wide are stacked. (c). Checking the BAZ coverage. Stations with a poor BAZ coverage, which is defined here as the number of stacked BAZ bands with data less than 12 out of the 36 possible bands, or there is a gap of  $180^\circ$  or greater in the BAZ coverage, are not used in the study. (d). Manually checking the RFs especially the clarity of the peak of the maximum stacking energy. The azimuthal variation of the  $P$  to  $S$  converted waves should be clear, smooth, and coherent, and stations with significant bifurcations and sharp offsets of the  $P$  to  $S$  conversions are rejected.

Some temporary stations have BAZ bands with only a few or no events in the  $180\text{--}360^\circ$  BAZ range (Figure 2), and thus including the RFs in the BAZ range of  $180\text{--}360^\circ$  may generate results with large uncertainties. Because the arrival time of the  $P_{m,s}$  and  $P_s$  has a period of  $180^\circ$ , for these stations, we only use RFs in the BAZ band of  $0\text{--}180^\circ$  to extract the anisotropy parameters.

While some of the previous studies on crustal anisotropy also used the transverse RFs (TRFs; H. Liu & Niu, 2012; Z. Liu & Park, 2017; Park & Levin, 2016; Sun et al., 2012; Q. Wang et al., 2016), a visual inspection of the TRFs suggests that the arrival corresponding to the Moho on the TRFs has a SNR that is much lower than that on the radial RFs, probably due to the thick, strongly attenuative, and structurally complex crust beneath the Tibetan Plateau. The fact that most of the stations are portable rather than permanent ones (e.g., Z. Liu & Park, 2017) and thus have a limited number of events also contributes to the low SNR on the TRFs (supporting information Figure S1). Therefore, only radial RFs are used in the study. Additionally, some previous RF-based crustal anisotropy studies (e.g., Levin & Park, 1998) consider time shifts on the direct  $P$  wave due to crustal anisotropy. Because of the steep angle of incidence and the fact that the variation of arrival time on  $P$  wave is usually much smaller than that of  $S$  wave, we conclude that the influence of  $V_p$  anisotropy on the resulting crustal  $V_s$  anisotropy is negligible.

Two approaches, fitting arrival times and stacking of amplitudes at predicted  $P_{m,s}$  arrival times from candidate  $\phi$  and  $\delta t$  pairs, are utilized to measure the crustal anisotropy parameters. For the first approach, we employ equation (1) and adopt a nonlinear least squares fitting procedure to fit the  $P$  to  $S$  conversion arrival times relative to the direct  $P$  wave (Kong et al., 2016). In the second approach, a grid search is performed to obtain the optimal pair of parameters corresponding to the maximum stacking amplitude. Due to the fact that the southeastern Tibetan Plateau possesses a thick crust and significant crustal anisotropy (Kong et al., 2016), the searching range for  $t_0$  is set as  $4.5\text{--}9.0$  s with a step of  $0.1$  s, that for  $\phi$  is  $-90^\circ\text{--}90^\circ$  with an increment of  $1^\circ$ , and that for  $\delta t$  is  $0.0\text{--}1.5$  s with a time interval of  $0.05$  s. Most stations yield statistically consistent results from the two approaches. For these stations, the averaged results from the two approaches are adopted. For stations with large difference between the two approaches (the difference in  $\phi$  is greater than  $15^\circ$ , or that in  $\delta t$  is greater than  $0.15$  s), results from the  $P_{m,s}$  moveout fitting are used because we have found that this approach usually produces more stable results. This is mostly because the amplitudes of the  $P_{m,s}$  phase used by the second approach vary more significantly than the arrival times (Han et al., 2017). In addition, the significant trade-off between the crustal anisotropy, tilted axis of symmetry, and dipping interfaces may lead to variations in the stacking amplitude, making it difficult to reliably extract anisotropy using stacking amplitude. An example of single layered azimuthal anisotropy measurement using the two approaches is shown in Figure 3.

### 3.3. Measurement of Double Layered Anisotropy

Anisotropy above an intracrustal interface can be quantified by the layer-stripping method (Kong et al., 2016; Rumpker et al., 2014) beneath stations that clearly display such an interface. Because the  $P_s$  exhibits a characteristic sinusoidal variation with the BAZ, azimuthal anisotropy above the intracrustal interface can be obtained using the azimuthal moveout of the  $P_s$  phase by applying the single layer method described above. The  $P_{m,s}$  arrival times are affected by two anisotropic layers and thus reflect an integrated effect of anisotropy in both the upper and lower layers. As demonstrated in the examples shown in Figure 4, once the upper layer anisotropy parameters are determined, their contributions to the whole crustal anisotropy measured by the  $P_{m,s}$  can be removed to obtain the  $\phi$  and  $\delta t$  of the lower layer.

### 3.4. Evaluation of the Uncertainties of Crustal Anisotropy Measurements

We apply the bootstrap resampling technique (Efron & Irani, 1986; K. H. Liu & Gao, 2010; Vetterling et al., 1992) to evaluate the mean and standard deviation (SD) of the  $\phi$  and  $\delta t$  of a given station. For a given bootstrap integration,  $1-1/e = 63\%$  RFs are randomly selected, and about 60% of the chosen ones are used twice so

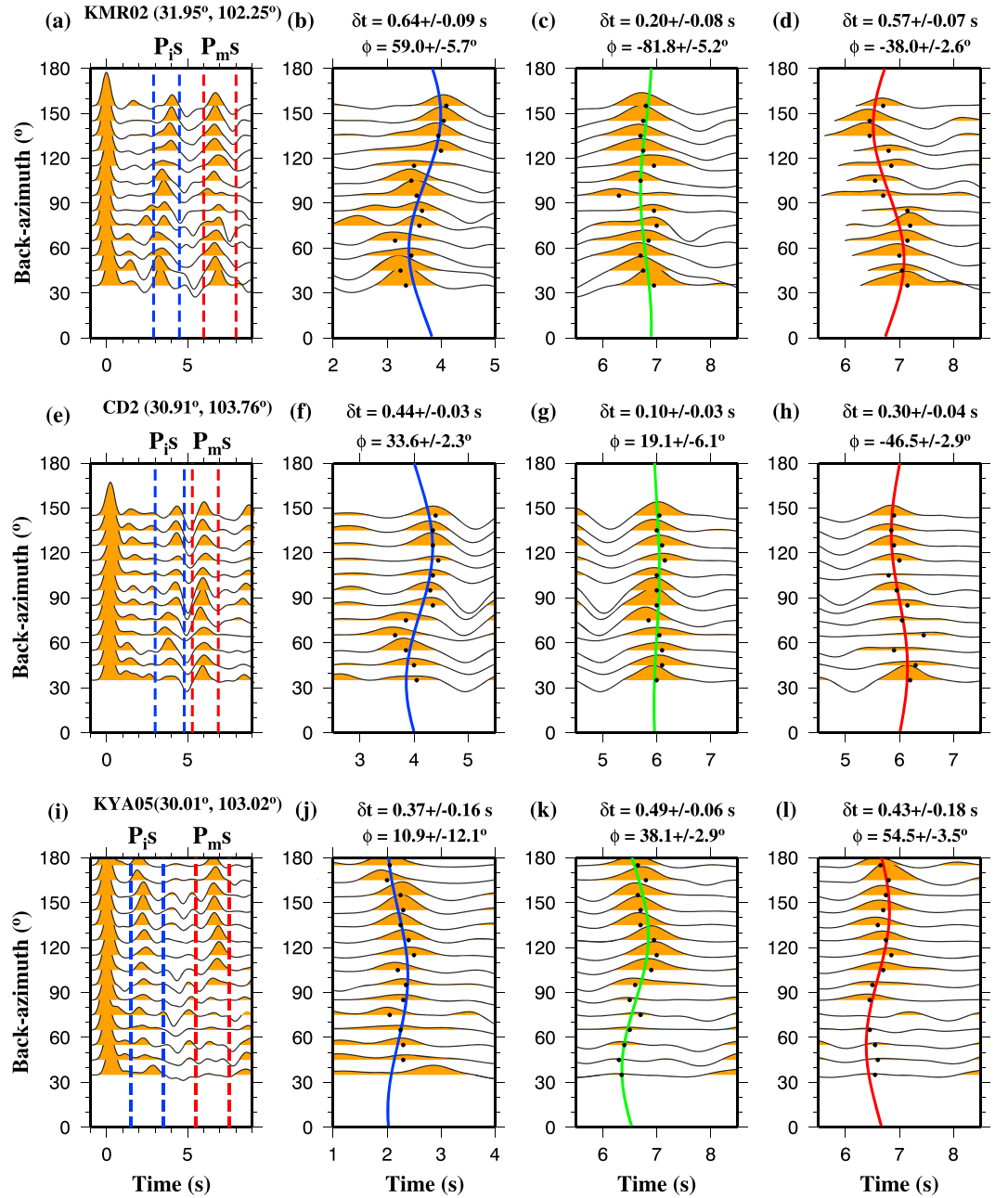


**Figure 4.** Double layered crustal anisotropy measurements at stations KMR02 (a)–(d), CD2 (e)–(h), and KYA05 (i)–(l). (a), (e), and (i) are the bin-averaged receiver functions plotted against the back azimuth showing the  $P_{ms}$  (between the two red dashed lines) and  $P_{1s}$  (between the two blue dashed lines) arrivals. The blue curve in (b), (f), and (j) is the theoretical moveout computed using the optimal anisotropy parameters from the  $P_{1s}$  phase; the green curve in (c), (g), and (k) is the theoretical moveout computed using the optimal anisotropy parameters from the  $P_{ms}$  phase; and the red curve in (d), (h), and (l) is the theoretical moveout computed after correcting the  $P_{ms}$  parameters with those obtained from the  $P_{1s}$  phase.

that the number of RFs is the same as that of the original set (K. H. Liu et al., 2003). The resulting SDs after 10 iterations for the two individual parameters are weighted to compute a combined SD for the station according to the following equation

$$\sigma = \frac{\sigma_{\delta t}}{1.0} + \frac{\sigma_{\phi}}{90.0}, \quad (2)$$

where  $\sigma_{\delta t}$  is the linear SD for  $\delta t$  and  $\sigma_{\phi}$  is the circular SD of  $\phi$ . Stations with a  $\sigma \geq 0.4$  are excluded in the analysis.

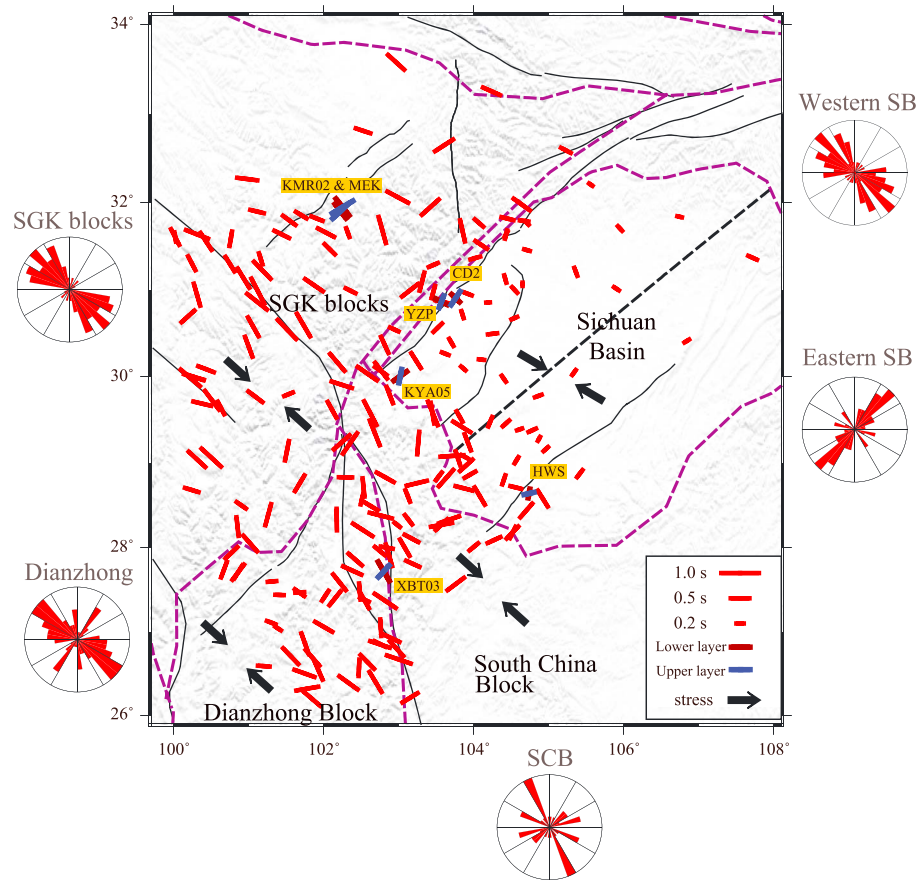


**Figure 5.** Crustal anisotropy measurements from this study (red bars). The length and orientation of the bars represent the  $\delta t$  and  $\phi$  measurements, respectively. For the seven stations with double layered anisotropy, the blue and purple bars represent the upper layer and lower layer anisotropy, respectively. The black dashed line separates the Sichuan Basin into two subunits, and the rose diagrams denote the distribution of the  $\phi$  values in each of the five subareas (SB = Sichuan Basin; SCB = South China Block). The thick black arrows show the mean maximum horizontal compressional stress direction (Heidbach et al., 2016). SGK = Songpan-Ganzi-Kangding.

### 3.5. Computation of Average $V_s$ Anisotropy

The resulting  $\delta t$  can be used to estimate the average crustal  $V_s$  anisotropy using

$$A_{V_s} = \frac{\delta t \cdot V_s}{H} = \frac{\delta t \cdot V_p}{H \cdot k}, \quad (3)$$

where  $A_{V_s}$  is the average  $V_s$  anisotropy in the crust,  $V_p$  (6.1 km/s) and  $V_s$  are the average  $P$  velocity and  $S$  velocity, respectively,  $k$  is the crustal  $V_p/V_s$  ratio, and  $H$  is the crustal thickness obtained by a previous study (Q. Liu et al., 2014).

## 4. Results

Among the 344 stations analyzed, 201 stations have reliable single layered and 7 stations have double layered anisotropy parameters (Figures 5–6 and Tables S1–S2). Our measurements are generally consistent with those from previous results at most of the stations (Figures 1 and 5), but both the number of stations and the spatial coverage are significantly greater than the previous studies (Chen et al., 2013; Kong et al., 2016; Sun et al., 2012, 2015). The averaged  $\delta t$  is  $0.43 \pm 0.11$  s, which is about a half of the splitting times of  $\sim 1.0$  s from previous XKS splitting studies conducted in the area (e.g., Chang et al., 2008; Flesch et al., 2005; C. -Y. Wang et al., 2007, 2008). A sharp contrast in  $\delta t$  is revealed between the stable Sichuan Basin and the surrounding tectonically active areas (Figure 7). The mean  $\delta t$  for stations outside the Sichuan Basin is  $0.48 \pm 0.13$  s, which is about twice as large as that observed at stations in the basin ( $0.23 \pm 0.10$  s).

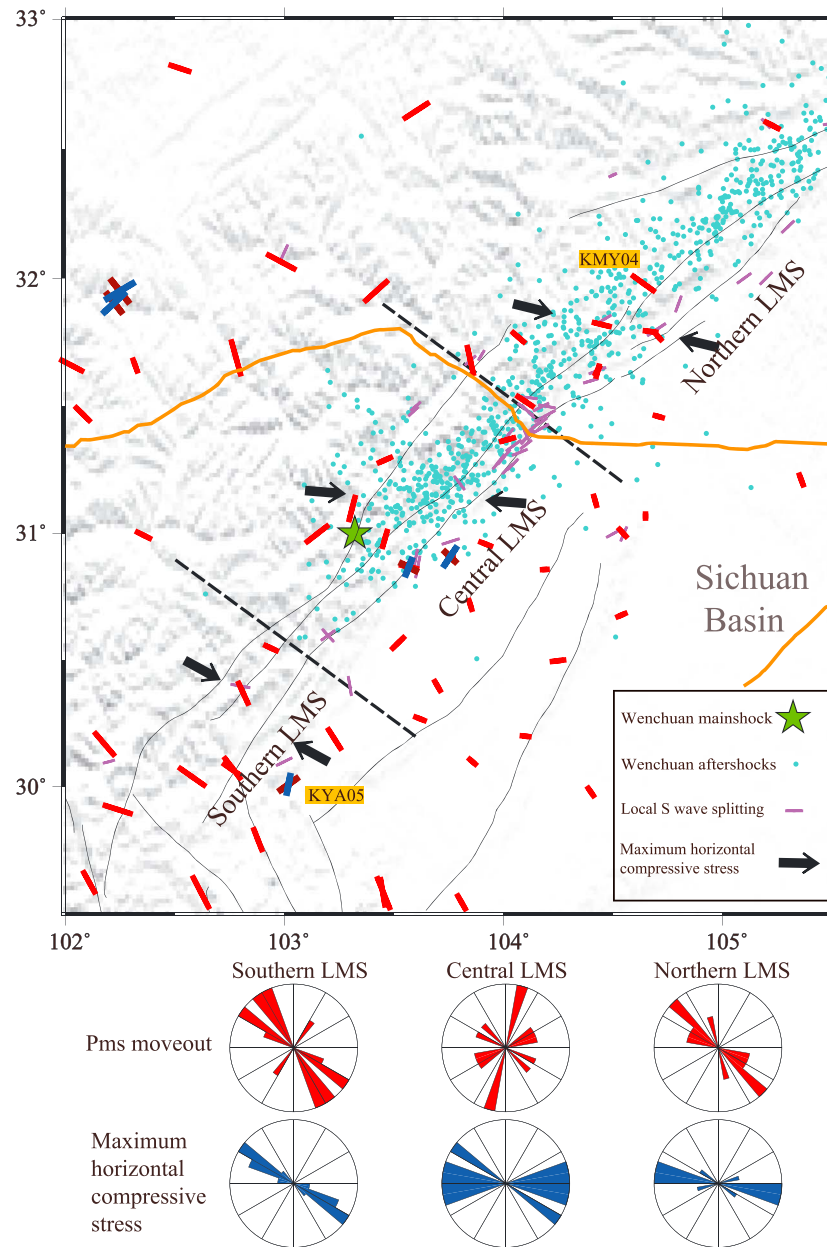


**Figure 6.** Crustal anisotropy measurements along the LMS fault zone and surrounding areas. The two dashed lines divide the fault zone into three segments. The green star is the initial rupture position of the Wenchuan earthquake, and light blue dots are aftershocks of the Wenchuan earthquake. Purple bars show the fast orientations from previous upper crustal anisotropy measurements from direct S wave splitting analyses (Y. Gao et al., 2013; Shi et al., 2013; Zheng et al., 2017). The thick black arrows denote the mean principal compressional stress (Heidbach et al., 2016). The area south of the orange line is dominated by high  $V_p/V_s$  measurements (greater than 1.8; C. -Y. Wang et al., 2010). The rose diagrams represent the fast orientations and regional maximum horizontal compressional stress in the three segments of the LMS fault zone. LMS = Longmenshan.

To facilitate discussion, the study area is divided into five subareas based on major geologic features, including the SGK blocks that occupy approximately the NW half of the study area, the Dianzhong Block that occupies the SW corner of the study area, the Sichuan Basin, the South China Block, and the LMS fault zone which separates the SGK blocks from the Sichuan Basin and consists of three (southern, central, and northern) segments. In addition, the Sichuan Basin is further divided into the western and eastern parts according to the characteristics of the anisotropy measurements (Figure 5). Table 1 shows the averaged anisotropy parameters and other relevant measurements for each of the subareas.

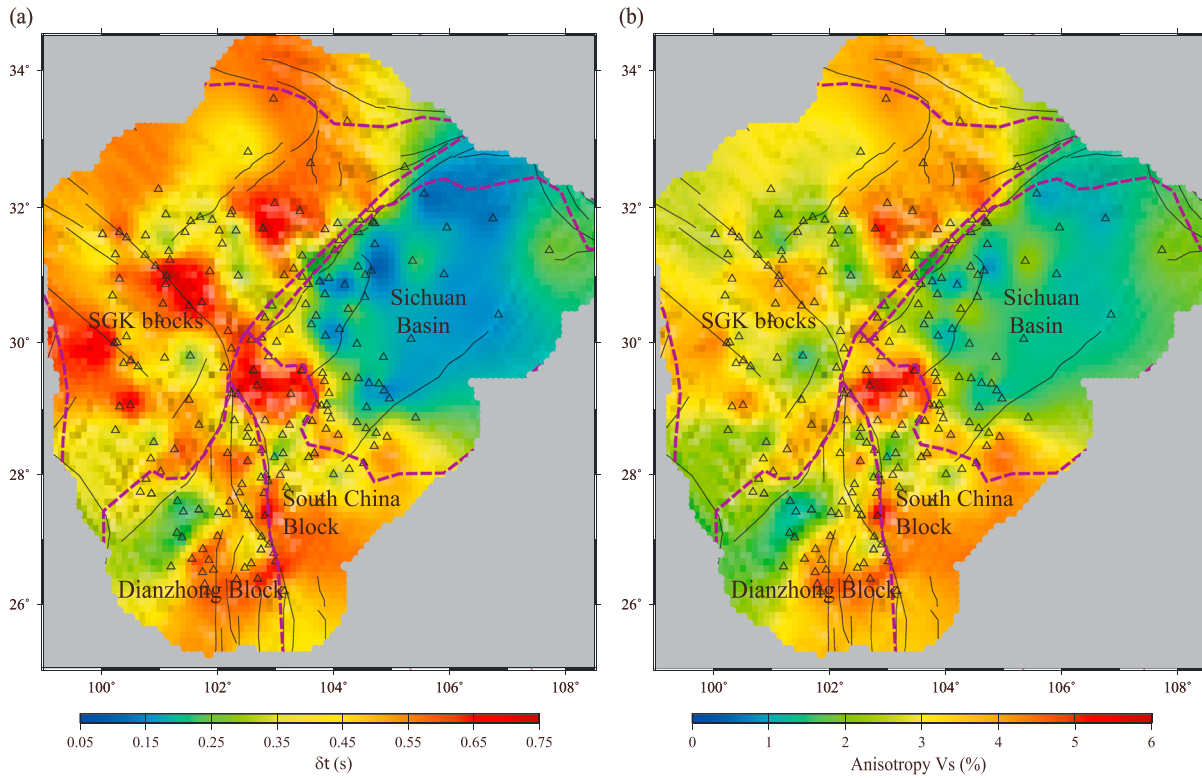


**Figure 7.** (a). Spatial distributions of the  $\delta t$  measurements. The individual  $\delta t$  observations at the stations (triangles) are fitted using a continuous curvature surface gridding algorithm (Smith & Wessel, 1990) with a tension factor of 0.5 and a sampling interval of  $0.1^\circ$ . (b). Spatial distributions of the  $V_s$  anisotropy according to equation (3). This quantity depends on Moho depth, crustal  $V_p/V_s$  ratio, and  $\delta t$ . The average  $P$  velocity in the crust is set as 6.1 km/s. SGK = Songpan-Ganzi-Kangding.

#### 4.1. SGK Blocks

The azimuthal anisotropy measurements beneath the SGK blocks demonstrate dominantly NW-SE  $\phi$  measurements, with an average  $\delta t$  value of  $0.51 \pm 0.12$  s. Similar to most other subareas, the resulting  $\phi$  measurements are mostly consistent with the strike of the active faults (Figure 5). Two nearby stations, KMR02 and MEK, exhibit the existence of double layered anisotropy, and the anisotropy parameters from the two stations are similar. The fast orientation of the upper layer is similar to the strike of the Longriba Fault, and that of the lower layer is orthogonal to the fault.

#### 4.2. The Dianzhong Block

The  $\phi$  measurements in the Dianzhong Block are dominantly NW-SE, which are inconsistent with the mostly N-S or NE-SW strike of the faults (Figure 5). The average  $\delta t$  value from stations located in the Dianzhong Block is

**Table 1**

*Averaged Anisotropy Parameters From  $P_m s$  Moveout and XKS Splitting, and APM and GPS Directions for the Subareas*

	SGK	Dianzhong	South China	Western SB	Eastern SB	Northern LMS	Central LMS	Southern LMS
$P_m s \phi$ ( $^\circ$ )	120.5	110.7	99.5	116.4	61.6	128.3	67.6	128.1
$P_m s \delta t$ (s)	0.51	0.47	0.48	0.22	0.31	0.40	0.37	0.46
XKS $\phi$ ( $^\circ$ )	117.8	91.9	108.5	136.8	94.3	123.0	137.9	162.7
XKS $\delta t$ (s)	1.03	0.93	0.94	0.93	0.83	0.95	0.77	0.79
APM ( $^\circ$ )	103	120	102	100	101	100	100	100
GPS ( $^\circ$ )	109	145	122	121	119	117	122	120

Note. SGK = Songpan-Ganzi-Kangding blocks; SB = Sichuan Basin; LMS = Longmenshan fault zone.

$0.47 \pm 0.13$  s. The western region of the Dianzhong Block demonstrates E-W fast orientations and anomalously small  $\delta t$  values that are less than 0.25 s (Figure 7).

#### 4.3. The LMS Fault Zone

Both the  $\phi$  and  $\delta t$  measurements show spatially systematic variations along the NE-SW trending LMS fault zone. The southern and northern segments of the fault zone show dominantly NW-SE  $\phi$  measurements, which are fault perpendicular. In contrast, the central segment is dominated by fault-parallel  $\phi$  measurements (Figure 6).

#### 4.4. The South China Block

The South China Block shows spatially varying  $\phi$  measurements which are mostly consistent with the trend of the northern and western edges of the block. The largest average  $\delta t$  value of  $0.63 \pm 0.08$  s in the study area is obtained at stations located at the intersection among the different tectonic units (Figure 7) and is responsible for the large average  $\delta t$  value of  $0.48 \pm 0.14$  s for the South China Block.

#### 4.5. The Sichuan Basin

The tectonically stable Sichuan Basin has the smallest mean  $\delta t$  of  $0.26 \pm 0.13$  s in the entire study area, with smaller  $\delta t$  values in the interior and larger values along the southern and western edges of the basin. A sharp contrast of the measured  $\phi$  is revealed between the western and eastern portions of the basin, with mostly NW-SE measurements for the western part and NE-SW for the eastern part (Figure 5).

## 5. Discussion

### 5.1. Alternative Causes of the Observed $P_m s$ Azimuthal Variation

The technique employed by this study assumes that the periodic moveout of the  $P$  to  $S$  converted phases is caused by a single layer of anisotropy with a horizontal axis of symmetry. While the periodic azimuthal variation of the  $P_m s$  (and  $P_t s$ ) arrival times with a  $180^\circ$  periodicity as well as the spatial consistency of the resulting crustal anisotropy (Figures 5–7) strongly suggest that the assumption of horizontal axis is probably valid, alternative explanation may exist for the observed moveout.

Z. Liu et al. (2015) and Z. Liu and Park (2017) suggested that the thick crust in Tibet may have strong layering that leads to  $P$  to  $S$  conversions from many internal interfaces, in addition to  $P$  to  $S$  conversions from the Moho. Using RFs from long-running permanent stations, Z. Liu and Park (2017) examined the situation where the effects of  $P$  to  $S$  conversion at the top and bottom of an anisotropic layer at the base of the crust could be mistaken for  $P$  to  $S$  conversion birefringence. While this is a possibility, the fact that only one robust  $P_m s$  arrival in the expected time window is observed at the vast majority of the stations (e.g., Figure 3) suggests that the resultant anisotropy reflects that of the whole crust rather than an anisotropic layer at the base of the crust. Similarly, the single robust  $P_m s$  arrival also suggests the absence of significant intracrustal layering at the majority of the stations. Such layering has been observed at long-running stations which usually have much more RFs and better azimuthal coverages than portable stations used in this study (e.g., Z. Liu et al., 2015).

To estimate the influence of a plunging fast axis on the measurements (e.g., Park & Levin, 2016; Schulte-Pelkum & Mahan, 2014), the RAYSUM code (Frederiksen & Bostock, 2000) is applied to generate the synthetic RFs (Figure S2). A fast axis with a large plunge ( $30^\circ$ ) from the horizontal plane has obvious effect on the amplitudes of the radial and TRFs, while the influence on the  $P_m s$  arrival times in the R components is insignificant. The reason is that the  $P$  to  $S$  conversions propagate near-vertically and polarize near-horizontally. The synthetic results indicate that the tilted fast axis does not significantly affect the measured crustal fast orientation and the splitting time. We conclude that the measurements obtained from the  $P_m s$  moveout can approximate the actual azimuthal anisotropy even in the presence of two lobed variation behavior of  $P$  to  $S$  conversions with a tilted axis of symmetry.

### 5.2. Stress-, Fracture-, and Crustal Flow-Induced Anisotropy in the LMS Fault Zone

The abrupt topographic relief across the LMS fault zone of about 500 km in length, where various studies have revealed distinct properties in different segments of the fault zone, suggests strong crustal deformation and complex geological structure. Geological studies (Arne et al., 1997; Burchfiel et al., 2008; Ma, 2002; Xu et al., 2009) revealed that significant variations of the surface topography and rock property exist beneath different segments of the LMS fault zone. A recent tomographic model (Z. Wang et al., 2017) further indicated that the fault zone is separated into three segments by two crustal bodies with anomalously low seismic velocity and high electric conductivity. In addition, Y. Gao et al. (2013) used direct  $S$  wave splitting analysis, which mainly

measures upper crustal anisotropy, to reveal a segmented pattern of the fast polarization orientations along the LMS fault zone (Figure 6). The upper crustal delay times beneath the LMS fault zone are generally less than 0.1 s revealed by previous studies using splitting of shear waves from local earthquakes (Chang et al., 2014; Ding et al., 2008; Zheng et al., 2017) and are significantly smaller than the  $\delta t$  of about 0.42 s obtained in the fault zone based on  $P$  to  $S$  conversions from the Moho, indicating that relative to the upper crust, the mid-lower crust is strongly anisotropic.

For the southern segment of the LMS fault zone (Figure 6), high  $V_p/V_s$  measurements with values ranging from 1.80 to 1.86 (Sun et al., 2015; C. -Y. Wang et al., 2010) are suggestive of the presence of partial melting in the mid-lower crust. Mineral physics studies (e.g., Christensen, 1996) suggested that  $V_p/V_s$  ratio in the crust can provide important constraints on crustal bulk average composition. Z. Zhang et al. (2009) suggested that high  $V_p/V_s$  ratio in the LMS fault zone may be caused by the overall mafic composition of the crust and the existence of fluids in the lower crust, probably moving southeastward beneath the SGK blocks from central Tibet (Clark & Royden, 2000). In addition, low resistivity (Bai et al., 2010) and low seismic velocities (Q. Liu et al., 2014) in the mid-lower crust beneath this area also imply the existence of crustal flow and partial melting. Based on the previous observations and the fact that the  $\phi$  observations in this segment of the LMS fault zone are mostly consistent with the anticipated SE-ward flow direction (Figure 5), we speculate that the principal cause of the observed crustal anisotropy in this area is the LPO of anisotropic minerals associated with the plastic flow in the mid-lower crust (Ji et al., 2015; Kong et al., 2016).

For the central segment of the LMS fault zone, the  $\phi$  measurements are dominantly consistent with the strike of the fault zone and also with the fast orientations obtained using splitting of shear waves from local earthquakes (Figure 6). The average  $\delta t$  is the smallest among the three segments of the fault zone (Table 1), which may imply the absence of strong mid-lower crustal flow beneath the central segment, although this study alone cannot rule out partial melting in the mid/lower crust. However, the normal  $V_s$  velocities in the mid-lower crust (Q. Liu et al., 2014; Z. Wang et al., 2017) observed in the area place doubts on the existence of significant crustal partial melting. Those characteristics can be explained by crustal anisotropy caused by fluid filled fractures in the fault zone. Double layered anisotropy is observed at two of the stations in this area (YZP and CD2), at which the fast orientation of the top layer is parallel to the strike of the fault zone, and that of the lower layer is orthogonal to it. Fluid-filled fractures in the fault zone can probably explain the NE-SW fast orientation of the upper layer. The 90° difference between the fast orientation of the upper and lower layers could be caused by complex crustal structure beneath the fault zone with a broad shear zone at depth.

Relative to the other segments of the LMS fault zone, the northern segment has low  $V_p/V_s$  values (ranging from 1.68 to 1.74; Sun et al., 2015), suggesting the absence of crustal flow. The consistency between the  $\phi$  measurements and the direction of the maximum horizontal compression (Figure 6), which is fault-orthogonal, suggests that NW-SE oriented extensional cracks are mostly responsible for the observed anisotropy. The lack of fault-parallel fast orientations in this area may imply that stress-induced anisotropy is significantly greater than that caused by fractures in the fault zone.

### 5.3. Evidence for Crustal Channel Flow Beneath the SGK Blocks

Similar to the southern section of the LMS fault zone, the  $\phi$  observations on the SGK blocks are dominantly fault-parallel (NW-SE) and the mean  $\delta t$  values are the largest among all the tectonic units (Table 1). As discussed above, the  $\delta t$  measured using the  $P_{ms}$  phase is mainly from the mid-lower crust. Crustal  $V_p/V_s$  studies (Chen et al., 2013; Sun et al., 2012, 2015; C. -Y. Wang et al., 2010) revealed that this area is dominated by higher than average  $V_p/V_s$  values, and magnetotelluric observations (e.g., Bai et al., 2010) showed a high electrical conductivity at lower crust depth beneath this area. In addition, the previously observed large-scale low velocity zone in the lower crust (e.g., Q. Liu et al., 2014; Yao et al., 2010) and strong radial anisotropy with  $V_{sh} > V_{sv}$  (Huang et al., 2010) are also consistent with the existence of mid-lower crustal flow. The dominantly NW-SE  $\phi$  observations in this area (Figure 5) provide additional evidence for the existence of the crustal channel flow system. The consistency between the  $\phi$  observations and the previously proposed southeast direction of the flow system (Clark & Royden, 2000) suggests that the LPO of amphibole in this area is Type II or Type III (Ko & Jung, 2015; Kong et al., 2016), for which the fast orientations are subparallel to the flow direction. In addition, some other possible mechanisms (Connolly & Podladchikov, 2013; Z. Liu et al., 2015) for generating anisotropy were proposed, such as fluid-flow in the lower crust, facilitated by vertical vein structures that cut through the internal shear zones, or vertically aligned rock volumes with alternating hydration levels,

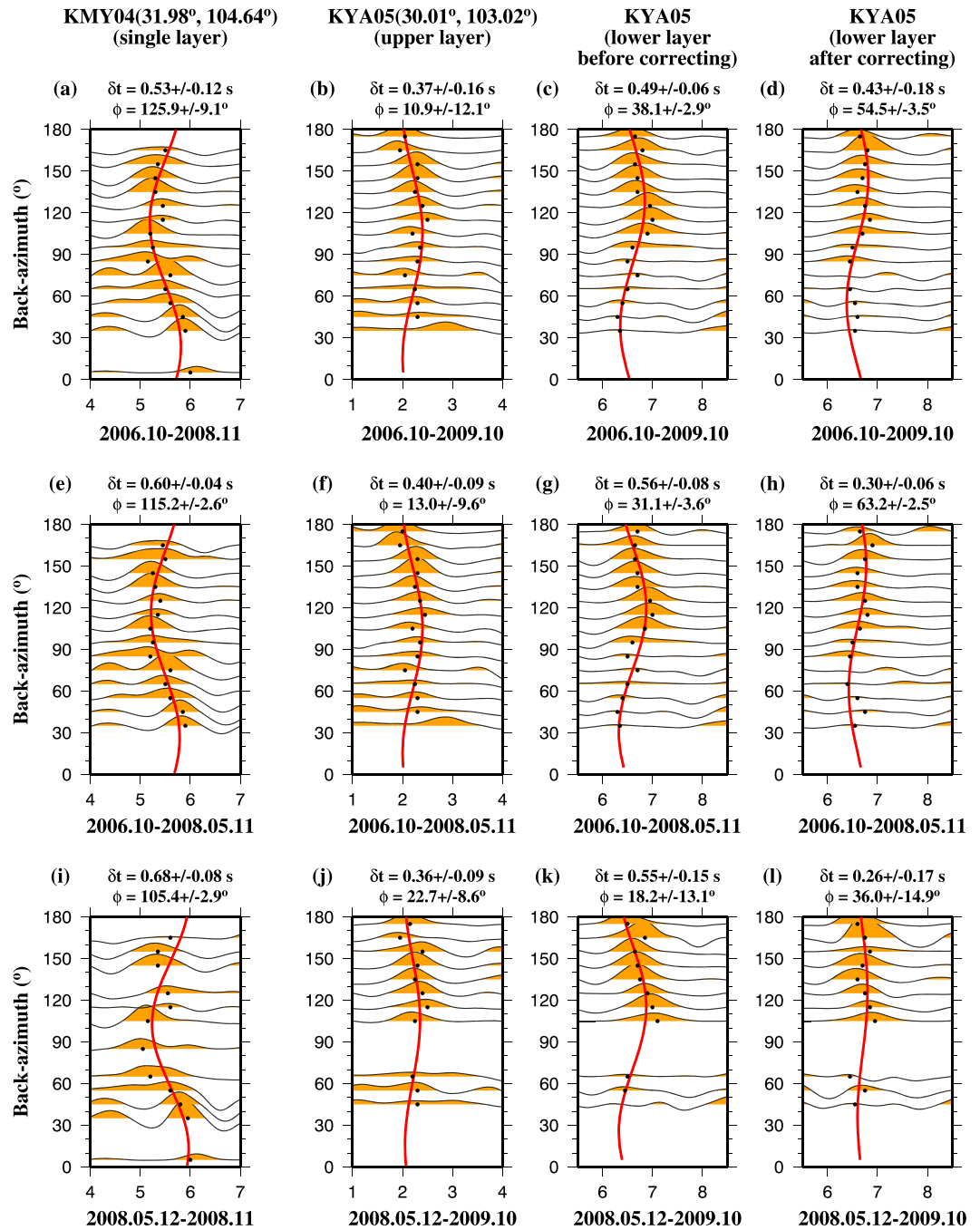


**Figure 8.** Pre- and post-Wenchuan earthquake crustal anisotropy measurements. The top (a-d), middle (e-h), and bottom (i-l) rows show all, pre-earthquake, and post-earthquake receiver functions plotted against the back azimuth, respectively. The first column from the left shows receiver functions from station KMY04 at which a single layered anisotropy model is revealed; the second to fourth columns are the same as the right-most three columns of Figure 4 but for station KYA05 which is characterized by a double layered crustal anisotropy model.

specifically alternating amphibolite and granulite rock masses. Besides faults in the upper crust and mid-lower crustal flow, shear-related mineral lineation may be a possible contributor to the observed anisotropy in the southeastern Tibetan Plateau. Ji et al. (2015) revealed that highly deformed fabrics with a subvertical foliation plane formed by compressional folding can lead to significant crustal anisotropy originating from anisotropic minerals. The resulting fast orientations are in the foliation plane and parallel to the lineation direction for a vertically propagating S wave (Ko & Jung, 2015).

#### 5.4. Crustal Anisotropy from Regional Compression in the Dianzhong Block

The  $\phi$  measurements in the Dianzhong Block are inconsistent with the strike of the active faults but are comparable to the maximum horizontal compressional stress, suggesting that extensional fluid-saturated microcracks associated with the regional compression is mostly responsible for the observed anisotropy. The measured  $\delta t$  values in the area between 26°N and 27°N show significant variations relative to the surrounding stations. Because results from GPS,  $P_m$ s moveout, and XKS splitting are measures of surface velocity vectors, crustal anisotropy, and upper mantle anisotropy, respectively, the discrepancies among the three types of measurements obtained in most part of the Dianzhong Block (Table 1) suggest that crustal and mantle deformation are largely decoupled. A recent study (Yang et al., 2018) has revealed widespread rotations of maximum compressional stress in the upper crust and significant differences between upper crustal stress field and seismic anisotropy. Similar to this study, Yang et al. (2018) support a decoupled deformation between the crust and upper mantle by a series of detachments, during crustal thickening resulted from the resistance to eastward expansion of the plateau by the rigid Sichuan Basin.

#### 5.5. Contrasting Crustal Anisotropy Between Western and Eastern Sichuan Basin

The tectonically stable Sichuan Basin, beneath which a thick and strong lithosphere is revealed (e.g., Hu et al., 2011, Shan et al., 2014), has the smallest average  $\delta t$  in the entire study area (Figure 7 and Table 1), implying that the observed crustal anisotropy is closely associated with the degree of crustal deformation which is in turn related to lithospheric strength and the magnitude of the deformation induced by the stress field. Near the southwestern edge of the basin, the  $\delta t$  measurements are larger than those observed in the interior of the basin, and the  $\phi$  measurements show an edge-parallel pattern, which reflects the effect of major boundary faults.

A sharp contrast in the observed  $\phi$  measurements is revealed between the western and eastern parts of the basin, with dominantly NW-SE  $\phi$  values for the western and NE-SW for the eastern parts of the basin (Figure 5). The  $\phi$  values in the former are consistent with the direction of the principal compressional stress, suggesting that the observed anisotropy could be explained as extensional cracks related to the regional compression. For the eastern part, on the other hand, the  $\phi$  values are consistent with the strike of the Huayingshan Fault, which may suggest a close relationship between the observed crustal anisotropy and fractures in the fault zone.

#### 5.6. Possible Effects of the Wenchuan Earthquake on Crustal Anisotropy

Many shear wave splitting studies using local earthquakes, which occur mostly in the seismogenic zone in the upper crust, have detected significant temporal changes in the splitting parameters associated with major earthquakes (e.g., Chang et al., 2014, Crampin et al., 1999, Y. Gao & Crampin, 2003). Similar changes in both the fast orientation and splitting time have been revealed before and after the Wenchuan earthquake occurred in the central segment of the LMS fault zone (Ding et al., 2008).

In the LMS fault zone, shear wave splitting from local earthquakes that are confined in the depth range of 5–15 km in the crust is mainly caused by microcracks in the upper crust (Ding et al., 2008; Y. Gao et al., 2013; Shi et al., 2013). As described in section 5.2, the upper crustal delay times from the local earthquakes are generally less than 0.1 s and are significantly smaller than the delay times of about 0.42 s obtained from  $P_m$ s moveout, indicating that the mid-lower crust is strongly anisotropic relative to the upper crust. In order to explore the possible impact of the Wenchuan earthquake on the anisotropy of the whole crust quantified by the  $P_m$ s moveout, we perform anisotropy analysis using RFs recorded before and after the earthquake for two of the permanent stations (KMY04 and KYA05), which have recorded the maximum amount of useful data among all the stations in the aftershock zone of the Wenchuan earthquake during both periods (Figure 6). As shown in Figure 8, station KMY04 exhibits a single layered and KYA05 shows a double layered model of anisotropy.

For station KMY04 situated in the northern segment of the LMS fault zone, at which splitting measurements using local earthquakes (focal depth 5–15 km; Ding et al., 2008) show a clear difference in both the fast orientations and splitting times before and after the earthquake, the pre- and post-earthquake whole crustal anisotropy parameters are similar (Figures 8e and 8i), indicating that although the earthquake has modified the anisotropic properties of the upper crust, its effects on whole crust anisotropy is below the detection level of the RF-based anisotropy analysis technique used in this study. In comparison, at station KYA05 located in the southern segment of the LMS fault zone, which was not ruptured by the Wenchuan mainshock, both the upper and lower layer anisotropy parameters are consistent before and after the Wenchuan earthquake, suggesting that the impact of the Wenchuan earthquake on upper and lower crustal anisotropy beneath the southern

segment is limited. This is consistent with previous Wenchuan earthquake studies (Shen et al., 2009; H. Zhang & Ge, 2010) which suggested that the rupture propagated unilaterally northeastward by about 300 km in the central and northern segments, while rupture propagation in the southern segment was limited.

## 6. Conclusions

$P$  to  $S$  converted phases from the Moho and from an intracrustal discontinuity are used to investigate crustal anisotropy beneath the southeastern Tibetan Plateau and adjacent areas, with unprecedented spatial coverage. Our results reveal that the  $\phi$  measurements observed in the vicinity of major active faults are dominantly consistent with the strike of the faults. A sharp contrast in  $\delta t$  between the plateau region and the Sichuan Basin indicates that crustal anisotropy is mostly related to the degree of crustal deformation which is a function of stress magnitude and lithospheric strength. Differences in anisotropy parameters obtained from XKS splitting,  $P_m$ s moveout, and local shear wave splitting suggest that the mid-lower crust is highly anisotropic, and crustal anisotropy is an important contributing factor to previously observed XKS splitting.

The observed crustal anisotropy in the southern segment of the LMS fault zone and the SGK blocks, when combined with the larger than normal  $V_p/V_s$  observations, supports the existence of crustal flow moving from central Tibet toward the southeast. In contrast, crustal anisotropy underneath the central segment of the LMS fault zone is mostly the result of fluid filled fractures, and fault-orthogonal extensional cracks in the upper crust beneath the northern segment of the LMS fault zone are mostly responsible for the observed anisotropy. The results show significant differences in crustal anisotropy between the western and eastern Sichuan Basin, and no detectable variation in whole crustal anisotropy is inferred from RFs recorded before and after the  $M_w$  7.9 Wenchuan earthquake.

## References

### Acknowledgments

The waveform data were provided by the Data Management Center of China National Seismic Network at Institute of Geophysics, China Earthquake Administration. All the receiver function waveforms in Seismic Analysis Codes (SAC) format used in the study can be accessed from <http://web.mst.edu/%7Esgao/TibetCrust>. We thank M. Sun and T. Wang for assistance with reformatting the RFs, and Y. Gao for discussion. Critical reviews by J. Park and an anonymous reviewer significantly improved the manuscript. This work is supported by the National Key Research and Development Program of China (grant 2017FYC1500200 to Z.D.), the National Natural Science Foundation of China (grants 41474088 and 41774061 to L.C.), the China Scholarship Council to T.Z., and the United States National Science Foundation (grants 0911346, 1321656, and 1830644 to K.L. and S.G.).

- Arne, D., Worley, B., Wilson, C., Chen, S., Foster, D., Luo, Z., et al. (1997). Differential exhumation in response to episodic thrusting along the eastern margin of the Tibetan Plateau. *Tectonophysics*, 280, 239–256. [https://doi.org/10.1016/S0040-1951\(97\)00040-1](https://doi.org/10.1016/S0040-1951(97)00040-1)
- Bai, D., Unsworth, M. J., Meju, M. A., Ma, X., Teng, J., Kong, X., et al. (2010). Crustal deformation of the eastern Tibetan Plateau revealed by magnetotelluric imaging. *Nature Geoscience*, 3(5), 358–362. <https://doi.org/10.1038/NGEO830>
- Bendick, R., & Flesch, L. (2007). Reconciling lithospheric deformation and lower crustal flow beneath central Tibet. *Geology*, 35(10), 895–898. <https://doi.org/10.1130/G23714A.1>
- Brownlee, S. J., Schulte-Pelkum, V., Raju, A., Mahan, K., & Condit, C. (2017). Characteristics of deep crustal seismic anisotropy from a compilation of rock elasticity tensors and their expression in receiver functions. *Tectonics*, 36, 1835–1857. <https://doi.org/10.1002/2017TC004625>
- Burchfiel, B. C., Royden, L. H., van der Hilst, R. D., Hager, B. H., Chen, Z., King, R. W., et al. (2008). A geological and geophysical context for the Wenchuan earthquake of 12 May 2008. *Sichuan, People's Republic of China. GSA Today*, 18(7), 4–11. <https://doi.org/10.1130/GSATG18A.1>
- Chang, L., Ding, Z., & Wang, C. (2014). Variations of shear wave splitting in the 2013 Lushan  $M_s$  7.0 earthquake region. *Science in China Series D: Earth Sciences*, 57(9), 2045–2052. <https://doi.org/10.1007/s11430-014-4866-8>
- Chang, L., Wang, C.-Y., & Ding, Z. (2008). Seismic anisotropy of upper mantle in Sichuan and adjacent regions. *Science in China, Series D: Earth Sciences*, 51(12), 1683–1693. <https://doi.org/10.1007/s11430-008-0147-8>
- Chen, Y., Zhang, Z., Sun, C., & Badal, J. (2013). Crustal anisotropy from Moho converted Ps wave splitting analysis and geodynamic implications beneath the eastern margin of Tibet and surrounding regions. *Gondwana Research*, 24(3–4), 946–957. <https://doi.org/10.1016/j.gr.2012.04.003>
- Christensen, N. I. (1996). Poisson's ratio and crustal seismology. *Journal of Geophysical Research*, 101(B2), 3139–3156. <https://doi.org/10.1029/95JB03446>
- Clark, M. K., & Royden, L. H. (2000). Topographic ooze: Building the eastern margin of Tibet by lower crustal flow. *Geology*, 28(8), 703–706. [https://doi.org/10.1130/0091-7613\(2000\)28<703:TOBTEM>2.0.CO;2](https://doi.org/10.1130/0091-7613(2000)28<703:TOBTEM>2.0.CO;2)
- Connolly, J. A. D., & Podladchikov, Y. Y. (2013). A hydromechanical model for lower crustal fluid flow. In D. E. Harlov & H. Austrheim (Eds.), *Metasomatism and the Chemical Transformation of Rock* (pp. 599–658). Berlin Heidelberg: Springer.
- Copley, A. (2008). Kinematics and dynamics of the southeastern margin of the Tibetan Plateau. *Geophysical Journal International*, 174(3), 1081–1100. <https://doi.org/10.1111/j.1365-246X.2008.03853.x>
- Crampin, S. (1987). Geological and industrial implications of extensive-dilatancy anisotropy. *Nature*, 328, 491–496. <https://doi.org/10.1038/328491a0>
- Crampin, S., Evans, R., Ucer, B., Doyle, M., Davis, J. P., Yegorkina, G. V., & Miller, A. (1980). Observations of dilatancy-induced polarization anomalies and earthquake prediction. *Nature*, 286(5776), 874–877. <https://doi.org/10.1038/286874a0>
- Crampin, S., & Gao, Y. (2008). A review of the new geophysics: A new understanding of pre-fracturing deformation in the crack-critical crust with implications for hydrocarbon production. *Petroleum Science*, 5(1), 1–12. <https://doi.org/10.1007/s12182-008-0001-9>
- Crampin, S., & Peacock, S. (2008). A review of the current understanding of seismic shear-wave splitting in the Earth's crust and common fallacies in interpretation. *Wave Motion*, 45(6), 675–722. <https://doi.org/10.1016/j.wavemoti.2008.01.003>
- Crampin, S., Volti, T., & Stefansson, R. (1999). A successfully stress forecast earthquake. *Geophysical Journal International*, 138(1), F1–F5. <https://doi.org/10.1046/j.1365-246X.1999.00891.x>
- Crampin, S., & Zatsepin, S. V. (1997). Modelling the compliance of crustal rock-II: Response to temporal changes before earthquakes. *Geophysical Journal International*, 129(3), 495–506. <https://doi.org/10.1111/j.1365-246X.1997.tb04489.x>
- Ding, Z., Wu, Y., Wang, H., Zhou, X., & Li, G. (2008). Variations of shear wave splitting in the 2008 Wenchuan earthquake region. *Science in China, Series D: Earth Sciences*, 51(12), 1712–1716. <https://doi.org/10.1007/s11430-008-0141-1>
- Efron, B., & Irani, R. (1986). Bootstrap methods for standard errors, confidence intervals, and other measures of statistical accuracy. *Statistical Science*, 1(1), 54–75. <https://doi.org/10.1214/ss/1177013815>

- England, P., & Houseman, G. (1986). Finite strain calculations of continental deformation: Comparison with the India-Asia collision zone. *Journal of Geophysical Research*, *91*(B3), 3664–3676. <https://doi.org/10.1029/JB091iB03p03664>
- Flesch, L. M., Holt, W. E., Silver, P. G., Stephenson, M., Wang, C.-Y., & Chan, W. W. (2005). Constraining the extent of crust-mantle coupling in central Asia using GPS, geologic, and shear wave splitting data. *Earth and Planetary Science Letters*, *238*(1-2), 248–268. <https://doi.org/10.1016/j.epsl.2005.06.023>
- Frederiksen, A. W., & Bostock, M. G. (2000). Modelling teleseismic waves in dipping anisotropic structures. *Geophysical Journal International*, *142*(2), 401–412. <https://doi.org/10.1046/j.1365-246X.2000.00090.x>
- Gan, W., Zhang, P., Shen, Z.-K., Niu, Z., Wang, M., Wan, Y., et al. (2007). Present-day crustal motion within the Tibetan Plateau inferred from GPS measurements. *Journal of Geophysical Research*, *112*, B08416. <https://doi.org/10.1029/2005JB004120>
- Gao, Y., & Crampin, S. (2003). Temporal variations of shear-wave splitting in field and laboratory in China. *Journal of Applied Geophysics*, *54*(3-4), 279–287. <https://doi.org/10.1016/j.jappgeo.2003.01.002>
- Gao, S. S., & Liu, K. H. (2014). Mantle transition zone discontinuities beneath the contiguous United States. *Journal of Geophysical Research: Solid Earth*, *119*, 6452–6468. <https://doi.org/10.1002/2014JB011253>
- Gao, Y., Wang, Q., Zhao, B., & Shi, Y. (2013). A rupture blank zone in middle south part of Longmenshan Faults: Effect after Lushan  $M_S$  7.0 earthquake of 20 April 2013 in Sichuan, China. *Science in China, Series D: Earth Sciences*, *57*(9), 2036–2044. <https://doi.org/10.1007/s11430-013-4646-x>
- Han, M., Li, J., Xu, X., & Hu, J. (2017). Analysis for crustal anisotropy beneath the southeastern margin of Tibet by stacking azimuthal receiver functions (in Chinese). *Chinese Journal of Geophysics*, *60*(12), 4537–4556. <https://doi.org/10.6038/cjg20171202>
- Heidbach, O., Rajabi, M., Reiter, K., Ziegler, M., & Team, W. (2016). World stress map database release 2016 GFZ data services, <https://doi.org/10.5880/WSM.2016.001>
- Hu, J., Xu, X., Yang, H., Wen, L., & Li, G. (2011). S receiver function analysis of the crustal and lithospheric structures beneath eastern Tibet. *Earth and Planetary Science Letters*, *306*(1-2), 77–85. <https://doi.org/10.1016/j.epsl.2011.03.034>
- Huang, H., Yao, H., & van der Hilst, R. D. (2010). Radial anisotropy in the crust of SE Tibet and SW China from ambient noise interferometry. *Geophysical Research Letters*, *37*, L21310. <https://doi.org/10.1029/2010GL044981>
- Ji, S., Shao, T., Michibayashi, K., Long, C., Wang, Q., Kondo, Y., et al. (2013). A new calibration of seismic velocities, anisotropy, fabrics, and elastic moduli of amphibole-rich rocks. *Journal of Geophysical Research: Solid Earth*, *118*, 4699–4728. <https://doi.org/10.1002/jgrb.50352>
- Ji, S., Shao, T., Michibayashi, K., Oya, S., Satsukawa, T., Wang, Q., et al. (2015). Magnitude and symmetry of seismic anisotropy in mica- and amphibole-bearing metamorphic rocks and implications for tectonic interpretation of seismic data from the southeast Tibetan Plateau. *Journal of Geophysical Research: Solid Earth*, *120*, 6404–6430. <https://doi.org/10.1002/2015JB012209>
- Ko, B., & Jung, H. (2015). Crystal preferred orientation of an amphibole experimentally deformed by simple shear. *Nature Communications*, *6*, 6586. <https://doi.org/10.1038/ncomms7586>
- Kong, F., Wu, J., Liu, K. H., & Gao, S. S. (2016). Crustal anisotropy and ductile flow beneath the eastern Tibetan Plateau and adjacent areas. *Earth and Planetary Science Letters*, *442*, 72–79. <https://doi.org/10.1016/j.epsl.2016.03.003>
- Kreemer, C. (2009). Absolute plate motions constrained by shear wave splitting orientations with implications for hotspot motions and mantle flow. *Journal of Geophysical Research*, *114*, B10405. <https://doi.org/10.1029/2009JB006416>
- Lev, E., Long, M. D., & Hilst, R. D. (2006). Seismic anisotropy in Eastern Tibet from shear wave splitting reveals changes in lithospheric deformation. *Earth and Planetary Science Letters*, *251*(3-4), 293–304. <https://doi.org/10.1016/j.epsl.2006.09.018>
- Levin, V., & Park, J. (1998). P-SH conversions in layered media with hexagonally symmetric anisotropy: A Cookbook. *Pure and Applied Geophysics*, *151*(2-4), 669–697. <https://doi.org/10.1007/s000240050136>
- Levin, V., & Park, J. (2000). Shear zones in the Proterozoic lithosphere of the Arabian Shield and the nature of the Hales discontinuity. *Tectonophysics*, *323*(3-4), 131–148. [https://doi.org/10.1016/S0040-1951\(00\)00105-0](https://doi.org/10.1016/S0040-1951(00)00105-0)
- Ligorria, J. P., & Ammon, C. J. (1999). Iterative deconvolution and receiver-function estimation. *Bulletin of the Seismological Society of America*, *89*(5), 1395–1400.
- Liu, K. H., & Gao, S. S. (2010). Spatial variations of crustal characteristics beneath the Hoggar swell, Algeria, revealed by systematic analyses of receiver functions from a single seismic station. *Geochemistry, Geophysics, Geosystems*, *11*, Q08011. <https://doi.org/10.1029/2010GC003091>
- Liu, K. H., Gao, S. S., Silver, P. G., & Zhang, Y. K. (2003). Mantle layering across central South America. *Journal of Geophysical Research*, *108*, 2510. <https://doi.org/10.1029/2002JB002208>
- Liu, H., & Niu, F. (2012). Estimating crustal seismic anisotropy with a joint analysis of radial and transverse receiver function data. *Geophysical Journal International*, *188*(1), 144–164. <https://doi.org/10.1111/j.1365-246X.2011.05249.x>
- Liu, Z., & Park, J. (2017). Seismic receiver function interpretation: Ps splitting or anisotropic underplating? *Geophysical Journal International*, *208*, 1332–1341. <https://doi.org/10.1093/gji/ggw455>
- Liu, Z., Park, J., & Rye, D. M. (2015). Crustal anisotropy in northeastern Tibetan Plateau inferred from receiver functions: Rock textures caused by metamorphic fluids and lower-crust flow? *Tectonophysics*, *661*, 66–80. <https://doi.org/10.1016/j.tecto.2015.08.006>
- Liu, Q., van der Hilst, R. D., Li, Y., Yao, H., Chen, J., Guo, B., et al. (2014). Eastward expansion of the Tibetan Plateau by crustal flow and strain partitioning across faults. *Nature Geoscience*, *7*(5), 361–365. <https://doi.org/10.1038/ngeo2130>
- Ma, L. (2002). *Geological Atlas of China (in Chinese)* (pp. 277–279). Beijing: Geological Publishing House.
- Mainprice, D., & Nicolas, A. (1989). Development of shape and lattice preferred orientations: Application to the seismic anisotropy of the lower crust. *Journal of Structural Geology*, *11*(1-2), 175–189. [https://doi.org/10.1016/0191-8141\(89\)90042-4](https://doi.org/10.1016/0191-8141(89)90042-4)
- McNamara, D. E., & Owens, T. J. (1993). Azimuthal shear wave velocity anisotropy in the Basin and Range Province using Moho Ps converted phases. *Journal of Geophysical Research*, *98*(B7), 12003–12017. <https://doi.org/10.1029/93JB00711>
- Meissner, R., Mooney, W. D., & Artemieva, I. (2002). Seismic anisotropy and mantle creep in young orogens. *Geophysical Journal International*, *149*(1), 1–14. <https://doi.org/10.1046/j.1365-246X.2002.01628.x>
- Molnar, P., & Tapponnier, P. (1975). Cenozoic tectonics of Asia: Effects of a continental collision. *Science*, *189*(4201), 419–426. <https://doi.org/10.1126/science.189.4201.419>
- Nagaya, M., Oda, H., Akazawa, H., & Ishise, M. (2008). Receiver functions of seismic waves in layered anisotropic media: Application to the estimate of seismic anisotropy. *Bulletin of the Seismological Society of America*, *98*(6), 2990–3006. <https://doi.org/10.1785/0120080130>
- Park, J., & Levin, V. (2016). Anisotropic shear zones revealed by backazimuthal harmonics of teleseismic receiver functions. *Geophysical Journal International*, *207*, 1216–1243. <https://doi.org/10.1093/gji/ggw323>
- Royden, L. H., Burchfiel, B. C., King, R. W., Wang, E., Chen, Z., Shen, F., & Liu, Y. (1997). Surface deformation and lower crustal flow in eastern Tibet. *Science*, *276*(5313), 788–790. <https://doi.org/10.1126/science.276.5313.788>
- Rumpker, G., Kaviani, A., & Latifi, K. (2014). Ps-splitting analysis for multilayered anisotropic media by azimuthal stacking and layer stripping. *Geophysical Journal International*, *199*(1), 146–163. <https://doi.org/10.1093/gji/ggu154>

- Schulte-Pelkum, V., & Mahan, K. (2014). A method for mapping crustal deformation and anisotropy with receiver functions and first results from USArray. *Earth and Planetary Science Letters*, *402*, 221–233. <https://doi.org/10.1016/j.epsl.2014.01.050>
- Shan, B., Afonso, J. C., Yang, Y., Grose, C. J., Zheng, Y., Xiong, X., & Zhou, L. (2014). The thermochemical structure of the lithosphere and upper mantle beneath south China: Results from multiobservable probabilistic inversion. *Journal of Geophysical Research: Solid Earth*, *119*, 8417–8441. <https://doi.org/10.1002/2014JB011412>
- Shen, Z.-K., Sun, J., Zhang, P., Wan, Y., Wang, M., Burgmann, R., et al. (2009). Slip maxima at fault junctions and rupturing of barriers during the Wenchuan earthquake 2008. *Nature Geoscience*, *2*(10), 718–724. <https://doi.org/10.1038/ngeo636>
- Shi, Y., Gao, Y., Zhang, Y., Wang, H., & Yao, Z. (2013). Shear-wave splitting in the crust in Eastern Songpan-Ganzi block, Sichuan-Yunnan block and Western Sichuan Basin (in Chinese). *Chinese Journal of Geophysics*, *56*(2), 481–494. <https://doi.org/10.6038/cjg20130212>
- Shiomi, K., & Park, J. (2008). Structural features of the subducting slab beneath the Kii Peninsula, central Japan: Seismic evidence of slab segmentation, dehydration, and anisotropy. *Journal of Geophysical Research*, *113*, B10318. <https://doi.org/10.1029/2007JB005535>
- Silver, P. G. (1996). Seismic anisotropy beneath the continents: Probing the depths of geology. *Annual Review of Earth and Planetary Sciences*, *24*, 385–432. <https://doi.org/10.1146/annurev.earth.24.1.385>
- Smith, W., & Wessel, P. (1990). Gridding with continuous curvature splines in tension. *Geophysics*, *55*(3), 293–305. <https://doi.org/10.1190/1.1442837>
- Sun, Y., Liu, J., Zhou, K., Chen, B., & Guo, R. (2015). Crustal structure and deformation under the Longmenshan and its surroundings revealed by receiver function data. *Physics of the Earth and Planetary Interiors*, *244*, 11–22. <https://doi.org/10.1016/j.pepi.2015.04.005>
- Sun, Y., Niu, F., Liu, H., Chen, Y., & Liu, J. (2012). Crustal structure and deformation of the SE Tibetan Plateau revealed by receiver function data. *Earth and Planetary Science Letters*, *349–350*, 186–197. <https://doi.org/10.1016/j.epsl.2012.07.007>
- Tapponnier, P., Lacassin, R., Leloup, P. H., Scharer, U., Zhong, D., Wu, H., et al. (1990). The Ailao Shan/Red River metamorphic belt: Tertiary left-lateral shear between Indochina and South China. *Nature*, *343*, 431–437. <https://doi.org/10.1038/343431a0>
- Tapponnier, P., Xu, Z., Roger, F., Meyer, B., Arnaud, N., Wittlinger, G., & Yang, J. (2001). Oblique stepwise rise and growth of the Tibet Plateau. *Science*, *294*(5547), 1671–1677. <https://doi.org/10.1126/science.105978>
- Tatham, D. J., Lloyd, G. E., Butler, R. W. H., & Casey, M. (2008). Amphibole and lower crustal seismic properties. *Earth and Planetary Science Letters*, *267*(1–2), 118–128. <https://doi.org/10.1016/j.epsl.2007.11.042>
- Vetterling, W. T., Teukolsky, S. A., Press, W. H., & Flannery, B. P. (1992). *Numerical Recipes Example Book (Fortran) Second Edition*. New York: Cambridge University Press.
- Wang, C.-Y., Chang, L., Lv, Z., Qin, J., Su, W., Silver, P. G., & Flesch, L. M. (2007). Seismic anisotropy of upper mantle in eastern Tibetan Plateau and related crust-mantle coupling pattern. *Science in China, Series D: Earth Sciences*, *50*(8), 1150–1160. <https://doi.org/10.1007/s11430-007-0053-5>
- Wang, C.-Y., Flesch, L. M., Silver, P. G., Chang, L., & Chan, W. W. (2008). Evidence for mechanically coupled lithosphere in central Asia and resulting implications. *Geology*, *36*(5), 363–366. <https://doi.org/10.1130/G24450A.1>
- Wang, Q., Niu, F., Gao, Y., & Chen, Y. (2016). Crustal structure and deformation beneath the NE margin of the Tibetan Plateau constrained by teleseismic receiver function data. *Geophysical Journal International*, *204*(1), 167–179. <https://doi.org/10.1093/gji/ggv420>
- Wang, Z., Wang, X., Huang, R., & Liu, G. (2017). Deep structure imaging of multi-geophysical parameters and seismogenesis in the Longmenshan fault zone (in Chinese). *Chinese Journal of Geophysics*, *60*(6), 2068–2079. <https://doi.org/10.6038/cjg20170604>
- Wang, C.-Y., Zhu, L., Lou, H., Huang, B.-S., Yao, Z., & Luo, X. (2010). Crustal thicknesses and Poisson's ratios in the eastern Tibetan Plateau and their tectonic implications. *Journal of Geophysical Research*, *115*, B11301. <https://doi.org/10.1029/2010JB007527>
- Xu, X., Wen, X., Yu, G., Chen, G., Klinger, Y., Hubbard, J., & Shaw, J. (2009). Coseismic reverse- and oblique-slip surface faulting generated by the 2008  $M_W$  7.9 Wenchuan earthquake, China. *Geology*, *37*(6), 515–518. <https://doi.org/10.1130/G25462A.1>
- Yang, Y., Liang, C., Fang, L., Su, J., & Hua, Q. (2018). A comprehensive analysis on the stress field and seismic anisotropy in eastern Tibet. *Tectonics*, *37*, 1648–1657. <https://doi.org/10.1029/2018TC005011>
- Yang, Y., & Liu, M. (2009). Crustal thickening and lateral extrusion during the Indo-Asian collision: A 3D viscous flow model. *Tectonophysics*, *465*(1–4), 128–135. <https://doi.org/10.1016/j.tecto.2008.11.002>
- Yao, H., van der Hilst, R. D., & Montagner, J.-P. (2010). Heterogeneity and anisotropy of the lithosphere of SE Tibet from surface wave array tomography. *Journal of Geophysical Research*, *115*, B12307. <https://doi.org/10.1029/2009JB007142>
- Zhang, H., Cheng, H., Jin, Y., Luo, G., Wang, J., Yuen, A. D., & Shi, Y. (2016). The implications of regional microseismic activities: A lesson from 2008  $M_S$  8.0 Wenchuan earthquake. *Physics of the Earth and Planetary Interiors*, *261*, 107–117. <https://doi.org/10.1016/j.pepi.2016.06.006>
- Zhang, H., & Ge, Z. (2010). Tracking the rupture of the 2008 Wenchuan earthquake by using the relative back-projection method. *Bulletin of the Seismological Society of America*, *100*(5B), 2551–2560. <https://doi.org/10.1785/0120090243>
- Zhang, Z., Wang, Y., Chen, Y., Houseman, G. A., Tian, X., Wang, E., & Teng, J. (2009). Crustal structure across Longmenshan fault belt from passive source seismic profiling. *Geophysical Research Letters*, *36*, L17310. <https://doi.org/10.1029/2009GL039580>
- Zheng, T., Ding, Z., Chang, L., Zheng, C., Zhang, H., & Li, D. (2017). S-wave splitting in upper crust near the scientific drilling WFS-3 at the Wenchuan earthquake fault zone (in Chinese). *Chinese Journal of Geophysics*, *60*(5), 1690–1702. <https://doi.org/10.6038/cjg20170507>